Journal of Catalysis 271 (2010) 358–369

Contents lists available at ScienceDirect

Journal of Catalysis

journal homepage: www.elsevier.com/locate/jcat

# A novel synthesis route for bimetallic CoCr–MCM-41 catalysts with higher metal loadings. Their application in the high yield, selective synthesis of Single-Wall Carbon Nanotubes

Codruta Zoican Loebick [a], Sungchul Lee [a], Salim Derrouiche [a], Mark Schwab [a], Yuan Chen [b], Gary L. Haller [a], Lisa Pfefferle [a,*]

[a] Yale University, Department of Chemical Engineering, 9 Hillhouse Avenue, Rm. 300, New Haven, CT 06511, United States
[b] Nangyang Technological University, School of Chemical and Biochemical Engineering, Singapore 637453, Singapore

ARTICLE INFO

*Article history:*
Received 2 November 2009
Revised 7 January 2010
Accepted 18 February 2010
Available online 27 March 2010

*Keywords:*
SWNT
Cobalt
Chromium
MCM-41
Incorporation
Grafting

ABSTRACT

We present a study on CoCr–MCM-41 catalysts with stable nm-sized particles. The focus is their promoting effect on the synthesis of Single-Wall Carbon Nanotubes (SWNT).

Bimetallic CoCr–MCM-41 catalysts were synthesized by combined grafting and incorporation of metals in the framework. This synthesis allowed an increase in the maximum metal loading in the MCM-41 framework while maintaining nm-sized Co particles stable in high-temperature reactive environments. The SWNT yield was increased by more than 100% from the Co–MCM-41 catalyst.

Cobalt is responsible for SWNT nucleation. The role of chromium is to anchor small cobalt particles during reduction and prevent their sintering into large unreactive particles. A larger fraction of the cobalt in the bimetallic catalysts becomes available for the SWNT synthesis when compared to the monometallic one, leading to a significant yield increase. Another effect of the addition of Cr was a shift of the SWNT diameter distribution to smaller nanotubes.



## 1. Introduction

Since the discovery of carbon nanotubes, significant research in the field of catalysis has been dedicated to attaining high yield and selectivity in their synthesis by use of various catalytic systems [1,2]. Many of these research efforts have been directed at Single-Wall Carbon Nanotubes (SWNT). These interests were fueled by the wide range of potential applications for these systems particularly in the field of nanoelectronics [3–5]. Commercial applications are still hindered by the lack of uniformity in these samples. By lack of uniformity, we imply variations in the diameter and structural properties of SWNT in a given sample. The structural properties of a nanotube are denoted by a pair of integers $(n, m)$ referring to the basis vectors of the underlying primitive lattice. Both the tube diameter and its electronic properties, i.e. whether it is semiconducting or metallic in nature, are given by the chiral vector [6,7].

Bimetallic catalytic systems have been shown to be an efficient way to obtain samples that are enriched in one or a few types of SWNT [8–13]. Studies of the role of each metal in SWNT synthesis are important. In many of these systems, one of the components is responsible for the nucleation and growth of SWNT, while the co-metal stabilizes small nucleating particles and possibly alters their morphology. For example, Resasco and coworkers have obtained narrow distributions of SWNT with a CoMo catalyst where the (6, 5) tube is predominant. Mo was shown to stabilize small Co domains [8].

We previously reported that addition of Cr influences the catalytic behavior of the Co–MCM-41 system in SWNT synthesis. Particularly for an equimolar ratio between the two metal components, we demonstrated increased selectivity and yield in the co-incorporated bimetallic systems (CoCr–MCM-41) when compared to the monometallic ones (Co–MCM-41). Certain SWNT identities were preferentially obtained in the bimetallic catalysts, and the mean diameter of the SWNT produced could be tuned through reaction conditions. We explained this performance through an anchoring effect of the Cr ions on the Co particles responsible for nanotubes nucleation. A second factor deemed responsible for the CoCr–MCM-41 catalytic performance was the MCM-41 support. The high surface area, well-ordered mesoporous MCM-41 support had an important role in producing systems with stable chemical and physical properties [14,15].

A decreased rate of Co particles sintering under the synthesis conditions was demonstrated. Sintering is undesirable since it creates large Co particles that are not thermodynamically or kinetically favorable for production of SWNT. In consequence, the fraction of Co in the catalyst that is involved in SWNT nucleation

* Corresponding author.
*E-mail address:* lisa.pfefferle@yale.edu (L. Pfefferle).

0021-9517/$ - see front matter © 2010 Elsevier Inc. All rights reserved.
doi:10.1016/j.jcat.2010.02.021

gets reduced. In fact, sintering poses a challenge for many catalytic systems, and SWNT synthesis is particularly affected due to the high reaction temperatures involved. An increase in the metal loading which should correlate with an increased yield of carbon nanotubes can actually lead to a decrease in both yield and selectivity due to increased sintering.

The amount of metal that can be loaded in the MCM-41 structure is as well limited by the stability of the structure. For example, a Co loading exceeding 4% can collapse the ordered MCM-41 structure greatly decreasing the efficiency of the catalysts in SWNT synthesis because sintering is no longer prevented by the well-ordered support [16,17].

In the Co–MCM-41 catalyst, the yield of carbon nanotubes increased with the Co concentration up to a 3% load [18]. This posed a challenge. The cobalt loading that would generate the highest yield of SWNT (3%) cannot be achieved in the bimetallic catalysts by isomorphous substitution without substantial loss of the template stability since an equivalent amount of Cr also needs to be loaded leading to a total metal load of 6%.

In the isomorphous substitution catalyst synthesis, high concentrations of transition cations substituted for silicon atoms are predicted to interfere with the stability of the template and/or the rate of cross-linking of the silica to disrupt the structure. Once the structure is formed, it remains stable as long as only the surface hydroxyls are reacted (as in the grafting process) which can accommodate higher metal loadings [19]. Based on this assumption, we propose an alternate route of synthesis for the bimetallic catalysts by combined grafting and isomorphous substitution, allowing for higher metal loading while still maintaining the structural stability of MCM-41. By this method, we were able to translate the formation of small, narrowly distributed particles to higher loadings of metal in the bimetallic catalysts and significantly affect the SWNT yield and selectivity resulting from these systems.

Stabilizing high loading Co catalysts with nm-sized particles stable to high temperatures in reactive environments can be generally attractive for other catalytic applications such as the Fischer Tropsch process, ethanol steam reforming, methanation or glycerol hydrogenolysis [20–23].

## 2. Experimental

### 2.1. Catalyst synthesis

The catalysts were synthesized in two distinct steps. In the first step, the monometallic Co–MCM-41 and Cr–MCM-41 were synthesized by isomorphous substitution of silicon atoms. The other metallic component of the catalytic system was added in a second synthesis step by grafting. This combined synthesis method was chosen for two reasons: first as discussed before, the incorporation of higher than 4% metal loadings in the MCM-41 structure leads to disruption of the structure stability. Second, if both metals would be added by subsequent grafting, the second grafting procedure can be less efficient due to the decrease of the available bonding sites on the silica surface. In the following, the synthesis will be discussed in the two separate steps.

#### 2.1.1. Synthesis of the monometallic catalysts by isomorphous substitution of silicon in the MCM-41 framework with Co or Cr

As base materials for all catalysts, two silica sources were used: Cab–O–Sil M-5 from Sigma–Aldrich and tetramethyl ammonium silicate (TMASi 10 wt.% silica) from Sachem Inc. The ratio between the soluble silica and total silica was 0.3. The total silica amount per batch of synthesized catalyst was 2.5 g. The metal sources used were $CoSO_4$ and $Cr(NO_3)_3$ both as a 6 wt.% solution in deionized water. The quantity of added metal source solution was determined such that each metal represented 3 wt.% of the total silica.

The templating material was a 20 wt.% surfactant solution with a 16 carbon atom alkyl chain length ($C_{16}H_{33}(CH_3)_3NBr$ which was ion exchanged with a Amberjet-400 (OH) resin from Sigma–Aldrich.

The silica sources and the metal solution were mixed for 30 min, then the surfactant solution as well as a couple of drops of Antifoam A concentrate (Sigma–Aldrich) was added. The mixing was continued for another hour, then the solution pH was adjusted to 11.5 using glacial acetic acid [24]. The synthesis solution was subsequently transferred into a polypropylene bottle and autoclaved at 115 °C for 6 days. After cooling to room temperature, the resulting solid was recovered by filtration, washed with deionized water, and dried over night at ambient conditions. The last step in the synthesis was calcination at 540 °C for 5 h under flowing air to remove the residual organics.

#### 2.1.2. Synthesis of the bimetallic catalysts by grafting through atomic layer deposition

The as-calcined monometallic catalysts (Co–MCM-41 and Cr–MCM-41) were grafted with a second metallic component (Cr on Co–MCM-41 and Co on Cr–MCM-41).

The metal precursors were Co(II) acetylacetonate and Cr(III) acetylacetonate (in quantities determined such as the metal loading of each metal on the MCM-41 would be 3 wt.%) dissolved in 150 mL of anhydrous toluene. The solution was refluxed at 110 °C for 3 h with nitrogen flowing through the apparatus to completely dissolve the precursor. The as-calcined monometallic catalysts (500 mg) were simultaneously suspended in 80 mL of anhydrous toluene and refluxed under flowing nitrogen to remove any adsorbed water. The precursor solution was then added to the monometallic catalyst suspension and refluxed for another 3 h under nitrogen. The reaction mixture was cooled, filtered and washed with toluene. The solids were dried and calcined in air at 540 °C.

Plain silica MCM-41 was also grafted with cobalt and with chromium by the same procedure as detailed above. The list of all synthesized catalysts is shown in Table 1.

### 2.2. Catalyst characterization

*Nitrogen Physisorption Isotherms* at 77 K were measured with a Quantachrome Autosorb-3b static volumetric instrument. Prior to measurement, the samples were outgased at 200 °C to a residual pressure below $10^{-4}$ Torr. A Baratron pressure transducer (0.001 Torr) was used for low pressure measurements. The specific surface area was calculated following the BET method. The pore size and pore size distribution were calculated by the BJH method using the desorption branch of the isotherm.

*Powder X-ray Diffraction* of the samples was recorded on a Bruker–Nonius Kappa CCD area detector X-ray diffractometer equipped with a fully integrated 4-circle goniometer and FR590 3 kW sealed tube generator.

*Temperature Programmed Reduction* (TPR) – About 100 mg of fresh catalyst was loaded into a quartz reactor and submitted to a programmed temperature rise in a flow at atmospheric pressure of 5% hydrogen diluted in argon. The reduction rates were continuously measured by monitoring the composition of the gas at the outlet of the reactor.

*Extended X-ray Absorption Fine Structure* (EXAFS) – X-ray absorption measurements were performed at the Co K-edge and at the Cr K-edge. The experiments were carried out on line X18B at the NSLS, 2.5 GeV storage ring, Brookhaven National Laboratory. Samples were pressed into self-supporting wafers and placed in a stainless steel cell equipped with Kapton windows, a gas inlet

**Table 1**
Synthesized catalysts.

| Catalyst | Synthesis method |
|---|---|
| CogCr–MCM-41 | 3 wt.% Co grafted on 3 wt.% Cr–MCM-41 synthesized by isomorphous substitution |
| CrgCo–MCM-41 | 3 wt.% Cr grafted on 3 wt.% Co–MCM-41 synthesized by isomorphous substitution |
| Co–MCM-41 | 3 wt.% Co–MCM-41 synthesized by isomorphous substitution |
| Cr–MCM-41 | 3 wt.% Cr–MCM-41 synthesized by isomorphous substitution |
| CogMCM-41 | 3 wt.% Co grafted on MCM-41 |
| CrgMCM-41 | 3 wt.% Cr grafted on MCM-41 |

and outlet, and a heating unit allowing in situ gas treatments. Details of the experimental procedure are given elsewhere [25].

### 2.3. SWNT synthesis

SWNT were synthesized by CO disproportionation using the cobalt-containing catalysts. Chromium ions alone cannot initiate the growth of carbon nanotubes since they do not reduce to zerovalent state under the conditions employed in this experiment; therefore, the monometallic Cr-containing catalysts were not used in the SWNT synthesis.

About 200 mg of catalyst was employed per batch. The catalyst was loaded in a quartz reactor with a 1.8-cm internal diameter, which was placed in a ceramic fiber radiant heater.

The synthesis was carried out in two main steps. The first step is the pre-reduction of the catalyst in hydrogen at atmospheric pressure and 700 °C at a flow rate of 1000 cc/min. In this step, the metal ions in the framework partially reduce their oxidation state. Without the pre-reduction step, cobalt is still reduced in CO, and nanotubes synthesis is still initiated. However, low carbon loadings are obtained with decreased selectivity for SWNT because the atomically dispersed Co ions are not easily available to CO [16–18]. Pre-reduction is followed by the reaction step when pure CO at 700 °C and 80 psi. is flowed through the system at a rate of 1000 cc/min. In this phase, the cobalt is further reduced, and clusters are formed that initiate the growth of SWNT as observed in earlier studies using in situ X-ray absorption spectroscopy [4].

### 2.4. SWNT characterization

*Thermal Gravimetric Analysis* (TGA) data were collected in a Setaram Setsys 1750 instrument under air flow. Samples were held at 150 °C in pure argon for 1 h to dehydrate before initiating the temperature program. The initial weight change in the sample was monitored between 150 and 1000 °C at 10 °C/min for two successive ramps. The second ramp was used as baseline correction for the first.

*Raman Spectroscopy* – Raman spectra of the as-synthesized SWNT samples were recorded using a Jasco LASER Raman Spectrophotometer NRS-3000 Series. Spectra were recorded using 785- and 532-nm excitation laser wavelengths. Each of the spectra represents an average of 10 scans taken on different points of the sample.

*Transmission Electron Microscopy* (TEM) – TEM images of the samples were recorded using a Tecnai F12 120 kV microscope. The sample, sonicated in ethanol, was dispersed prior to imaging on a holey carbon grid.

*Fluorescence spectroscopy* – In 10 mL of 1 wt.% sodium dodecyl benzene sulfonate in $D_2O$ was dispersed 0.5 mg of sample that has been treated with a NaOH solution to remove the silica framework and sonicated with a tip sonicator at 80% amplitude for 1 h. The suspension was then centrifuged at 100,000*g* for 1 h, and 80% of the supernatant was decanted for measurement. Photoluminescence (PL) maps were collected on a Jobin–Yvon Nanolog 3 spectrofluorometer equipped with an IGA NIR detector.

## 3. Results and discussion

### 3.1. Catalyst characterization

Nitrogen adsorption–desorption isotherms of the bimetallic catalysts and the corresponding BJH pore size distribution are shown in Fig. 1 and Table 2. A comparison is made with the incorporated monometallic catalysts that were used as base for adding the second metal component.

All isotherms show a sharp inflection at relative pressure $P/P_o$ in the range 0.3–0.4 characteristic of type IV isotherms [26]. In the pore size distribution plot (inset in Fig. 1), a narrow peak around 28 Å is indicative of uniform pore size. A note should be made that all measured isotherms are similar in shape to the siliceous MCM-41, showing good mesoporous structure to be retained during catalysts synthesis [27].

The bimetallic catalysts show an approximate 20% decrease in BET surface area when compared to the monometallic ones. Two factors can contribute to the surface area decrease. The higher metal loading independent of the synthesis method can decrease the surface area. Second, as a result of the grafting process, a decrease in the surface area occurs as a result of hydroxyl condensation. To support this second assumption, we collected nitrogen physisorption data for the CogMCM-41 catalyst (results not shown here). The resulting surface area was 1134 $m^2/g$, lower by about 17% than the

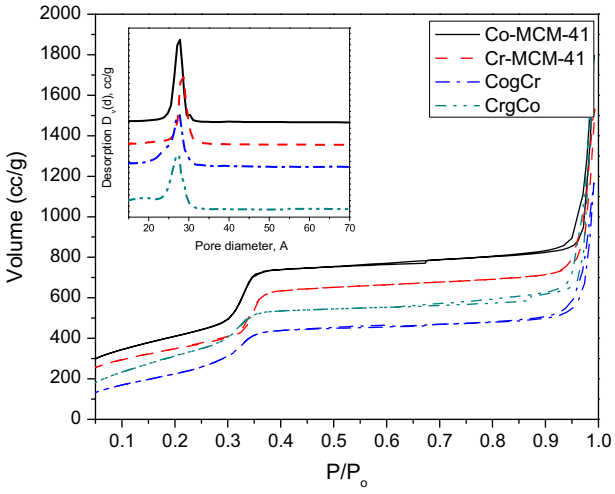


**Fig. 1.** $N_2$ adsorption–desorption isotherms of the Co–MCM-41, CogMCM-41, CogCr and CrgCo catalysts.

**Table 2**
Properties of monometallic and bimetallic catalysts obtained by nitrogen physisorption.

| Catalyst | Calculated metal loading (wt.%) | BET surface area ($m^2/g$) | Pore diameter (Å) |
|---|---|---|---|
| Co–MCM-41 | 3 | 1389 | 27.7 |
| Cr–MCM-41 | 3 | 1261 | 28.7 |
| CogCr | 6 | 1074 | 27.8 |
| CrgCo | 6 | 1036 | 27.3 |

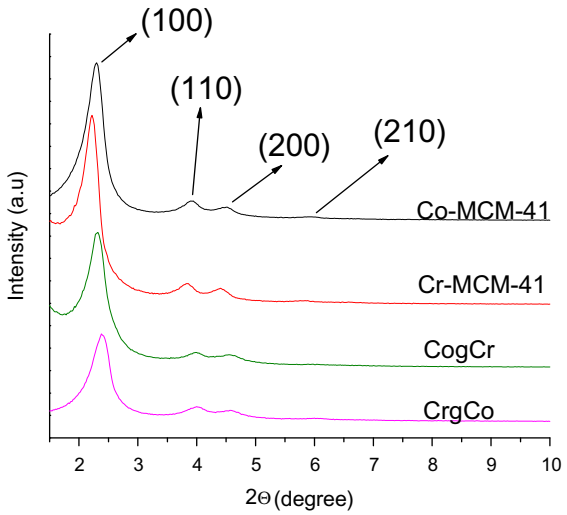


**Fig. 2.** XRD patterns of Co–MCM-41, Cr–MCM-41, CogCr and CrgCo.

Co–MCM-41 catalyst even though both catalysts had the same metal loading.

A decrease in pore size (around 0.4 Å for CrgCo and 0.9 Å for CogCr) is noted after grafting of the second metal. This can be attributed to pore surface reconstruction due to dehydroxylation rather than an additional layer of metal formed inside the pore, which would have led to a more significant shift on the pore diameter. We assume the grafted metal to be embedded in the pore wall, and this will be shown by TPR.

To assess the efficiency of our method, a catalyst containing 3% Co and 3% Cr was synthesized by isomorphous substitution of both metals in the MCM-41 framework. The surface area determined by nitrogen physisorption (Fig. S1 of Supporting information) was 521 $m^2$/g. This is less than 50% of the surface area of the bimetallic catalysts with the same loading synthesized by combined isomorphous substitution and grafting.

All powder XRD patterns (Fig. 2) exhibit four *hkl* diffraction peaks characteristic of the highly ordered structure of the MCM-41. The first peak in all patterns is related to the (1 0 0) plane of the template and has the highest intensity in all samples. In addition, the secondary reflections at higher $2\theta$ due to the (1 1 0), (2 0 0) and (2 1 0) planes are also recorded in all patterns and shown here. The (2 1 0) reflection is very weak. These peaks are characteristic for the long-range order of the mesoporous MCM-41 [28] (see Fig. 3).

Some decrease in the peak intensities can be noted in the bimetallic catalysts most likely due to the increase in the metal concentration. Nevertheless, the ordered structure of the MCM-41 template is demonstrated by XRD in the bimetallic catalysts. In contrast, the bimetallic catalyst synthesized by co-incorporation of the two metals at the same loading as the bimetallic CogCr and CrgCo catalysts did not show the higher angle reflection peaks. TEM images collected on this catalyst showed large crystals residing on the surface most likely unincorporated metal (Figs. S2 and S3 of the Supporting information).

TEM images of the as-synthesized bimetallic catalysts through combined incorporation and grafting are shown in Fig. 2. The images show uniform, well-defined structures. Hexagonal channels around 3 nm in diameter, characteristic of well-ordered MCM-41, are noted, in good agreement with the nitrogen physisorption results.

The reduction profiles of all catalysts are shown in Fig. 4. Both the Co–MCM-41 sample and the CogMCM-41 sample show reduction of Co ions at temperatures around 850 °C. This temperature is characteristic of the $Co^{2+}$ ions reduction to zerovalent state [14,16,17]. In the Co–MCM-41 catalyst, the Co ions are expected to be atomically dispersed within the silica pore wall, while in the CogMCM-41 catalyst, they are dispersed and anchored to the surface by Co–O–Si oxo bridges [14,16,17,29]. The elevated reduction temperature of the Co ions is indicative of good dispersion and incorporation/anchoring. Surface residing, undispersed Co oxides would reduce at lower temperature (under 400 °C) [30,31].

The Cr ions reduce at around 400–450 °C in the Cr–MCM-41 and CrgMCM-41 catalysts. We assume the initial oxidation state of the chromium in the catalyst to be 6+ for both the incorporated and the grafted samples [14,29]. In the Cr-containing monometallic catalysts (Cr–MCM-41 and CrgMCM-41), this was confirmed as well by the intense yellow color. The oxidation state reduces to 2+ during TPR. Further reduction is not thermodynamically favorable at the conditions employed in this experiment [32,33].

The reduction of both incorporated and grafted Co ions takes place at around the same temperature. This is surprising because grafted ions are on the surface of the silica pore wall, more accessible to hydrogen and in consequence more available for reduction. Since the reduction pattern of Co ions in both samples follows the same trend, we can assume that in Co–MCM-41 sample, the incorporated ions are close to the silica pore wall as opposed to its depth. This makes the stability against reduction of the incorporated ions close to the one of the grafted ions.

The different precursors used in the synthesis need to be taken into account. Acetylacetonates are very suitable for grafting procedures but cannot be used in the direct synthesis method due to

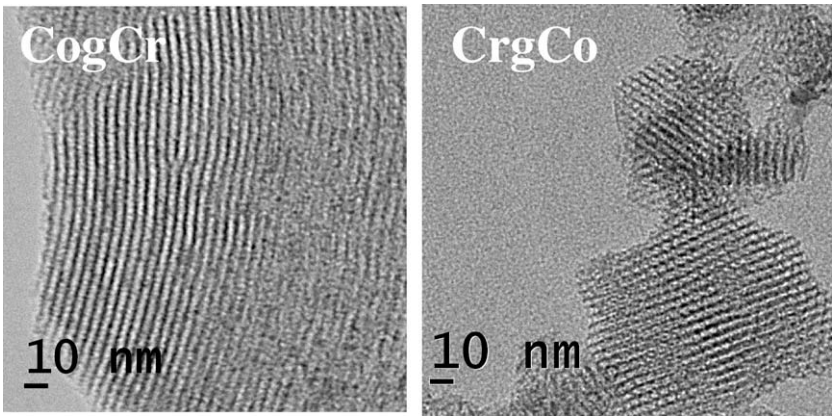


**Fig. 3.** TEM images of the as-synthesized bimetallic CogCr (left) and CrgCo (right) catalysts.

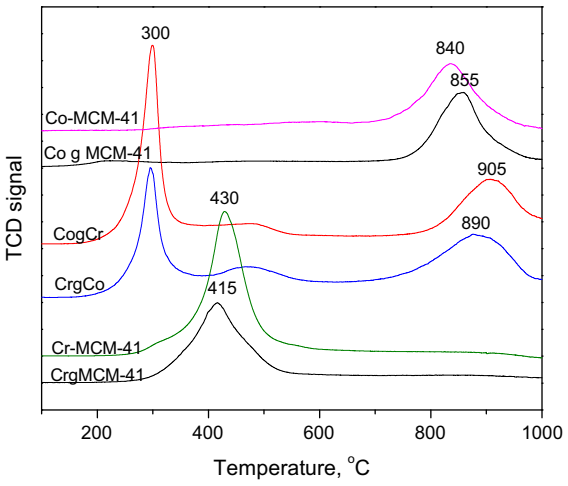


**Fig. 4.** Temperature Programmed Reduction (TPR) profiles of the Co–MCM-41, CoMCM-41, CogCr and CrgCo catalysts.

their insolubility in water. Use of organic precursors for synthesis of Co–MCM-41 instead of inorganic ones lead to a better dispersion of the metal ions in the framework, increasing their stability [34]. Both of these factors can have an effect on the reducibility and can explain why the grafted and incorporated samples have similar reduction temperatures.

In the bimetallic catalysts, two opposite effects are noted when comparing the reduction of the Co and Cr ions to the reduction of their monometallic counterpart. First, the reduction of the Cr ions takes place at a lower temperature (around 300 °C as opposed to 400–450 in the monometallic samples). Second, the maximum reduction rate of the Co ions is shifted to a higher temperature than in the monometallic catalysts. This behavior indicates a direct interaction between the Co and Cr ions in the framework. Most likely a $CoCrO_4$ mixed oxide type structure is formed. This interaction was observed in our previous studies by XAS measurements in co-incorporated CoCr–MCM-41 catalysts [14] as well as the current work. Resasco and coworkers showed the formation of similar mixed oxides structures in the synthesis of both CoMo and CoW bimetallic catalysts supported on $SiO_2$ [8,9]. The pattern noted in all these studies was reduction of the hexavalent metal (Cr, Mo, W) at lower temperature, while Co ions reduction shifted to higher temperature than in the corresponding monometallic catalysts.

Studies conducted on different chromium–cobalt spinels and mixed oxide compounds have shown Co to be an accelerant of the $Cr^{6+}$–$Cr^{2+}$ reduction [9,35]. This effect can only be seen if most Co and Cr ions are in close proximity in the silica template. Some weak reduction peaks around 450 °C observed in both bimetallic catalysts can be attributed to Cr ions that are not interacting with Co.

The reduced Cr ions act as anchoring sites for Co particles during reduction. This translates into a slowed kinetics of the Co ions reduction and implicitly an increase in their maximum reduction rate temperature [14]. In both bimetallic catalysts, the maximum reduction rate of the Co ions takes place at a temperature approximately 50 °C higher than the monometallic catalysts.

X-ray absorption spectroscopy can be used to unravel the electronic and structural properties of the catalysts at different stages in the SWNT synthesis process.

The XANES region of the EXAFS spectrum collected at the Co K-edge for the as-calcined catalysts and known references (cobalt oxides with different oxidation states and a commercial cobalt chromate reference) are showed in Fig. 5a and a detail of the pre-edge region is shown in Fig. 5b. All spectra are normalized

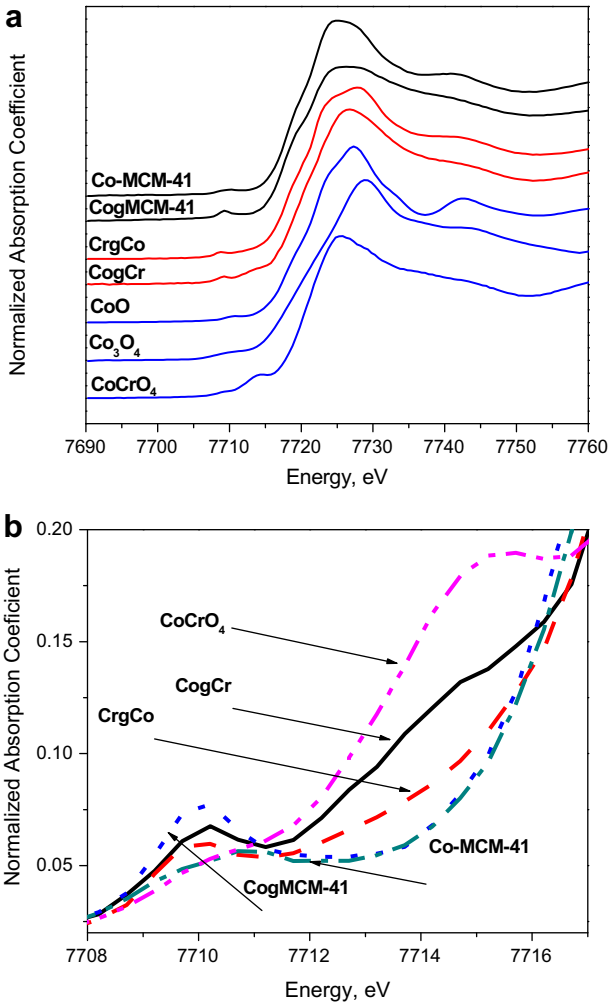


**Fig. 5.** (a) Co K-edge XANES spectra in the range 7690–7760 eV collected at the Co K-edge for the monometallic and bimetallic catalysts and references. (b) Detail of the pre-edge region.

by the jump height at the Co K-edge and calibrated using the cobalt foil standard edge energy at the first inflection point in the Co foil calibration spectrum at 7709 eV. The spectra of all catalysts were collected after dehydration under helium at 300 °C. The dehydration was necessary to remove all contributions that absorbed water can possibly have on the Co–O coordination number and white-line intensity.

A comparison between the XANES spectra for all synthesized catalysts and references shows major contributions from $Co^{2+}$. Lim and coworkers showed that in the Co–MCM-41 catalysts, the cobalt species consists of a mixture of tetrahedral and distorted tetrahedral coordination of cobalt atoms [36]. A fitting of the first Co–O coordination shell (Table S1 of Supporting information) was performed using the IFFEFIT software. Cobalt–oxygen paths from a known tetrahedrally coordinated compound (cobalt aluminate) were used and the single-scattering assumption was made. The resulting first shell coordination number was around 4 for all catalysts, confirming the mostly tetrahedral environment of the central Co atom.

We will further extend the discussion to the pre-edge region of the EXAFS spectra in Fig. 5b. In the monometallic samples and oxide references, the pre-edge peak at 7709 eV comes from the 1s–3d dipole forbidden transition in the central Co atom.

The bimetallic oxides have a different, distinct structure. Chaturvedi and coworkers [37–39] showed that two types of metal

atoms appear in a mixed metal oxide of the kind ($M_1M_2O_4$). Some occupy mixed $M_1$–O–$M_2$–O rings, while others are involved in monometallic M–O–M–O rings. Mixed metal oxides coordination is structurally different from monometallic oxides. When compared with the corresponding monometallic oxides, these mixed species were shown, for example, to have a higher density of states near the top of the valence bands.

An extra pre-edge feature appears in the $CoCrO_4$ reference at 7714 eV due to a 1s–4p electronic transition. This feature has not been identified in any of the monometallic Co catalysts. The bimetallic CogCr and CrgCo show a similar pre-edge feature, somewhat more intense for the CogCr catalyst as evident from Fig. 5b. This suggests that a mixed oxide-like coordination of Co and Cr forms in the bimetallic systems during catalyst synthesis. The pre-edge peak appearing at 7709 is present in the bimetallic catalysts and is more intense than in the $CoCrO_4$ reference compound. This likely indicates that not all of the two metals are in the mixed oxide coordination. However, they are in close proximity in the template, probably separated by no more than two or three oxygen atoms since the reducibility of the two metals is strongly affected when compared to the monometallic catalysts as shown by TPR. The mixed metal oxide coordination is present in both bimetallic oxides regardless of the synthesis route (which was grafted versus incorporated).

At the Cr K-edge (Fig. 6), all catalysts show a strong pre-edge feature at 5992 eV. This feature attributed to the 1s–3d dipole forbidden transition is very intense for a non-central symmetric environment of the Cr atom [40,41] such as the tetrahedral coordination in $CrO_3$ or $CoCrO_4$. No other major differences are noted between the monometallic and bimetallic catalysts. The monometallic and bimetallic oxide references ($CrO_3$ and $CoCrO_4$) have very similar XANES spectra as well. A Fourier transform of the EXAFS data was performed using the IFFEFIT software (Fig. S4 of Supporting information). The peak due to the first oxygen coordination shell of Cr is essentially at the same *R* value (1.6 Å) and has the same amplitude for all catalysts and references samples.

Another function of the EXAFS data is that it can be used as a base for determining the concentration of metal atoms in the framework [42]. The physical meaning of the edge step is the change in the absorption coefficient at the edge energy of one atom, which is directly related to the atom concentration. In order to calibrate the edge step with the metal concentration, we used a series of measurements of monometallic Co–MCM-41 and Cr–MCM-41 samples with known concentrations of Co and Cr. These samples were analyzed by ICP measurements at the Galbraith Laboratories, and the metal concentration was determined as well by TPR. With these three independent measurements, we were able to construct a plot of Co and Cr concentration versus edge jump. A note should be made that all these EXAFS measurements were performed at identical conditions with the measurements discussed in this paper. The ratios between TPR areas corresponding to Co and Cr ions reduction also correspond very well with the EXAFS approximation of the metal loading. Results are shown in Table 3.

All concentrations appear to be in a range that is close to the proposed theoretical values. These results show that we have successfully introduced higher loadings of metal (over 5.5% in both bimetallic catalysts) without disrupting the MCM-41 framework.

The loading of Co and Cr is higher in the bimetallic catalysts than in the monometallic Co–MCM-41 and Cr–MCM-41 that were used as base for grafting. Also, the loading of Co in the CogMCM-41 catalyst is higher than the calculated value. As shown by Wang et al. [19], during the grafting procedure, some loss of silica occurs due to refluxing in toluene, which can account for the increased metal load.

Pre-reduction of the catalyst samples under hydrogen plays an important role in the synthesis process. Its purpose is to mobilize the ions in the silica template, making them more susceptible to interaction with carbon monoxide in the reaction phase [25]. The pre-reduction temperature of catalysts in this study was based on the TPR profiles. It is the temperature of the onset of the Co ions reduction. We chose this temperature because it is high enough to partially reduce the Co ions in the framework but not sufficient for a complete reduction that can lead to further sintering of Co particles. Based on our previous experiments [15], the pre-reduction temperature does not influence the structure of the resultant SWNT; however, it does affect the yield. For this purpose, we have carried out SWNT synthesis experiments at 600, 700 and 800 °C while maintaining a constant reaction temperature of 700 °C. We have found the highest carbon yield was obtained at the 700 °C pre-reduction temperature (results not shown here).

XAFS spectroscopy is a useful spectroscopic technique that provides information on the electronic and structural properties of catalysts under reaction conditions. As a complement to TPR, we chose this technique to probe the changes that occur in the catalysts under hydrogen at the same conditions as those employed in our laboratory for the production of SWNT.

Fig. 7 shows the XANES region of the EXAFS spectrum collected for all cobalt-containing catalysts after isothermal reduction in hydrogen at 700 °C. The spectra collected for the Co foil was included for comparison. The shape and position of the pre-edge peak as well as the intensity of the white-line feature (a measure of the density of empty states at the Fermi level) can be compared with the Co foil. A higher degree of reduction is noted for the monometallic samples (Co–MCM-41 and CogMCM-41) based on the lower intensity of the white-line and the shape of the pre-edge peak similar to that of the Co foil. The bimetallic catalysts appear to be more resistant against reduction in agreement with the TPR results. The lesser reducibility is a consequence of the presence of the anchoring effect of Cr in the framework.

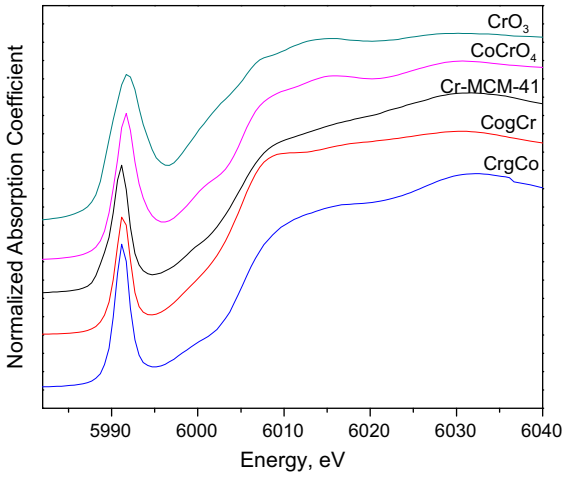


**Fig. 6.** Cr K-edge XANES spectra of the monometallic and bimetallic catalysts and known references.

**Table 3**
Metal loading determined from the EXAFS spectrum.

| Catalyst | Co concentration (wt.%) | Cr concentration (wt.%) |
|---|---|---|
| CogCr–MCM-41 | 2.78 | 2.70 |
| CrgCo–MCM-41 | 2.67 | 2.40 |
| CogMCM-41 | 3.23 | – |
| Co–MCM-41 | 2.46 | – |
| Cr–MCM-41 | – | 2.62 |

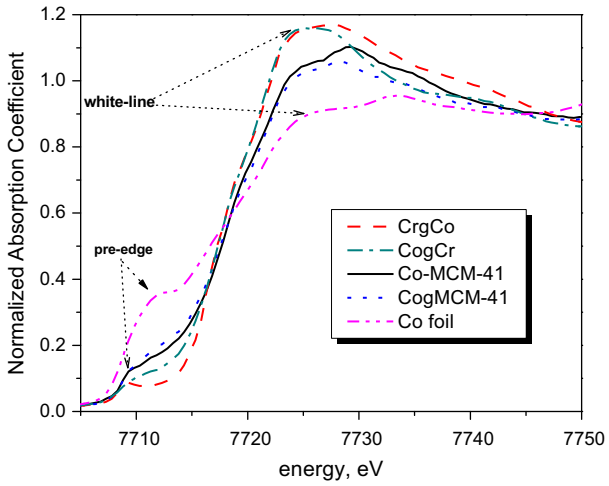


**Fig. 7.** Co K-edge XANES spectrum collected after isothermal reduction of catalysts at 700 °C.

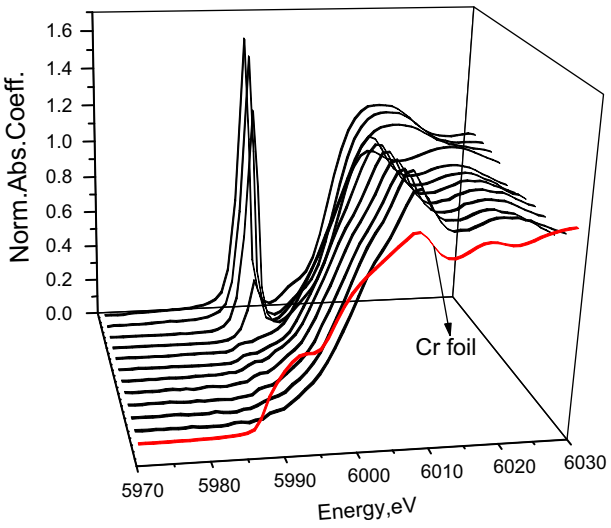


**Fig. 8.** Cr K-edge XANES data collected during the isothermal reduction with pure hydrogen at 700 °C of the CogCr catalyst.

A fit of the EXAFS data collected after the in situ reduction of the cobalt-containing catalysts was performed using the IFFEFIT program in a K-range from 2 to 12.5 $Å^{-1}$. Paths from both oxidized and metallic Co calculated from FEFF 6.0 were used in the fit. Data collected for the metallic Co foil and the Co oxides references were used to determine the value of the amplitude functions used for each path. The background was subtracted by means of cubic spline function. Fourier transforms were performed using a parametrized Kaiser Window between 2 and 10 $Å^{-1}$. Results are shown in Table 4.

Co–Co bonds were present in all catalysts. A lesser degree of reduction can be attributed to the bimetallic catalysts. Within the limits of the uncertainty, the central Co atom has on average 1–2 less neighboring Co atoms in its coordination sphere in the bimetallic catalysts than in the monometallic ones. The average Co–O first shell coordination number is also higher for the bimetallic catalysts than for the monometallic ones.

A note should be made that the coordination number determined from fitting should be corrected for the fraction of the reduced Co in the sample as the EXAFS spectrum is a volume average of species, both reduced and oxidized. The actual Co–Co coordination number might be somewhat larger than the one determined from the fit; however, the trend of the reduction among the different catalysts will not be changed.

The same isothermal reduction experiment was reproduced at the Cr K-edge. The chosen pre-reduction temperature exceeds the temperature range in which the Cr ions reduction takes place as noted from the TPR. At this temperature, all Cr-containing catalysts showed an identical behavior when exposed to hydrogen. As an example, the XANES data collected during the in situ reduction of the CrgCo catalyst is shown in Fig. 8. The same data collected for the CogCr catalyst and the Cr–MCM-41 catalyst are shown in Figs. S5 and S6 of Supporting Information.

The strong pre-edge feature characteristic to the $Cr^{6+}$ tetrahedral coordination gets completely suppressed during exposure to hydrogen. A positive shift in the main edge position is also indicative of the coordination change that occurs during reduction. The shape and main edge position of the final spectra (after reduction for 30 min at 700 °C) agrees with the presence of isolated pseudo octahedral $Cr^{2+}$ in all catalysts [32,43].

Co particles have a double role in the SWNT synthesis. First, they break the bonds of the carbon source and produce carbon atoms. Second, they act as solvents for carbon, initiating the formation of SWNT when supersaturation is reached. The size and conformation of the nucleating metal particle is the key factor in controlling the diameter and chirality of the resulting nanotubes. Metallic particles of about 0.6–0.7 nm are the smallest responsible for growth of well-ordered SWNT. At the opposite end, particles of over 2.5–3 nm are more likely to deposit layers of graphite than initiate the growth of SWNT [44,45].

EXAFS spectroscopy represents a good method for assessing the average size of the cobalt particles formed during SWNT growth. Since these particles are covered with carbon, their oxidation state is preserved during exposure to atmospheric air. An ex situ measurement of the as-reacted catalysts at the cobalt K-edge provides reliable information on the average particle size. The XANES portion of the EXAFS spectrum collected for the Co-containing catalysts after carbon deposition is shown in Fig. 9. A clear pre-edge peak characteristic of metallic Co is seen in all catalysts. The difference in intensity between the white-line of the reacted catalysts and the metal foil can be attributed to formation of cobalt–carbon bonds since the Co particles are saturated with carbon during SWNT synthesis. The radial distribution function (inset in Fig. 9) obtained by $K^2$ Fourier transform of the EXAFS data shows the major contribution from one backscatterer peak due to Co. The position of the main peak at 2.45 Å corresponds to the Co–Co bond.

A simulation of the EXAFS spectrum was performed under the same conditions employed for the fitting of the after-reduction data. The results are shown in Table 5. The data suggest that no di-

**Table 4**
Fitting results of the EXAFS data collected for the Co-containing catalysts after isothermal reduction at 700 °C.

| Catalyst | Average Co–O first shell coordination number | Co–O bond distance (Å) | Average Co–Co first shell coordination number | Co–Co bond distance (Å) |
|---|---|---|---|---|
| CogCr | 2.6 ± 0.6 | 1.85 | 1.0 ± 0.6 | 2.45 |
| CrgCo | 2.5 ± 0.8 | 1.85 | 1.9 ± 0.9 | 2.45 |
| CogMCM-41 | 1.7 ± 0.5 | 1.85 | 2.8 ± 0.5 | 2.45 |
| Co–MCM-41 | 1.4 ± 0.5 | 1.85 | 3.9 ± 0.8 | 2.45 |

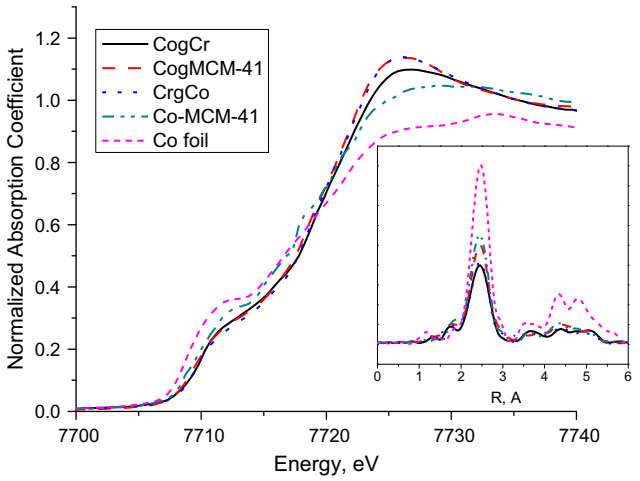


**Fig. 9.** XANES spectrum of the Co-containing catalysts after carbon deposition. Inset showing the radial distribution function ($0 < R > 6$ Å) after $K^2$-weighed Fourier transformation of the EXAFS data.

**Table 5**
Fitting results of the EXAFS data collected for the Co-containing catalysts after carbon deposition.

| Catalyst | Co–O first shell coordination number | Co–Co first shell coordination number | Estimated particle size (nm) |
|---|---|---|---|
| Co–MCM-41 | 0.58 ± 0.28 | 7.87 ± 0.45 | 1.51 |
| Co grafted on MCM-41 | 0.71 ± 0.63 | 7.55 ± 0.65 | 1.39 |
| Co grafted on Cr–MCM-41 | 0.88 ± 0.76 | 5.69 ± 0.77 | 0.92 |
| Cr grafted on Co–MCM-41 | 0.79 ± 0.49 | 5.75 ± 0.62 | 0.94 |

rect Co–Cr bonding takes place since the position and amplitude of the main bond is the same in all samples; indifferent to the presence of Cr.

Fittings made considering Co–Cr bond formation in the first coordination shell were, as expected, not consistent with the data.

In order to determine the approximate size of the Co clusters from the average first shell Co–Co coordination number, we built a (1 1 1)-truncated hemispherical cuboctahedron model [25]. The results obtained from this model are shown in Table 5. The resulting size of the Co particles in the bimetallic catalysts is on average 50% lower than for the monometallic ones. This comes as a result of the different rates of sintering of the Co particles due to the anchoring effect of Cr. The average diameter of the resultant nanotubes will be shown to shift to lower values in the bimetallic catalysts, which is an evidence for smaller Co particles being present.

There appears to be no major differences in the cobalt particle size between the two bimetallic catalysts. The bimetallic interaction effect is therefore valid independent of the synthesis route. The average particle size estimated from the cuboctahedron model is within the limits proposed to be favorable for SWNT growth in all catalysts [43,44].

As noted before, the particle size is crucial for the diameter of the resulting SWNT. It is possible that for a given particle size, the resulting SWNT can have the same diameter, but different chiral angles, i.e. different electronic properties. It has been shown that formation of nanotubes of the same diameter and different chirality does not occur in comparable proportion for catalyst particles of a given size. Growth is favored for the nanotube which has the lowest (kinetic) activation energy [46,47]. This induces production of high-angle chirality nanotubes. More important, this effect is much more pronounced when the diameter of the resultant nanotube is small. The growth mechanism of SWNT involves an initial carbon cap formation on the metal particle, which subsequently determines the geometry of the tube. When the metal particles are small, the number of possible cap structures that can form is also very small (the number of possible caps increases exponentially with the particle size). Out of these possible cap structures, those who favor higher chiral angle tubes tend to be more stable. For example, Miyauchi et al. [47] have shown that for a given particle size which can favor the production of either the (6, 5) or the (9, 1) tubes (both have the same diameter), the (6, 5) tube was predominant, while the (9, 1) tube had a very low abundance. It is therefore very important for a controlled production of SWNT to control the initiating particle size and reduce it to a size that is still large enough to grow defect-free SWNT but small enough to favor the production of only certain chiralities.

Resasco and coworkers have shown that for a bimetallic CoMo system supported on amorphous silica, Mo reacts with CO forming molybdenum carbide [8]. However, since the stable form of chromium carbide had Cr in a 3+ oxidation form and since most ions were seen to be in a 6+ oxidation state after carbon deposition and air exposure, we can assume that no chromium carbide was formed during SWNT synthesis.

### 3.2. Catalytic performance for SWNT synthesis

Thermal Gravimetric Analysis (TGA) is a widely employed method for estimating both the carbon yield and the selectivity of a catalyst toward SWNT compared to other byproducts of the synthesis, amorphous carbon, multiwalled carbon nanotubes (MWNT) and graphite [48–51]. The common interpretation for the TGA data attributes the 300–350 °C temperature interval to the oxidation of amorphous carbon, 400–650 °C to carbon nanotubes (single- and multi-walled) and higher temperatures (over 700 °C) to graphitic forms. Fig. 10 shows the inverted DTG spectra (derivative of the TG variation with temperature) collected for the as-reacted catalyst and normalized per mg carbon in the sample.

A slight weight increase at the beginning of the oxidation ramp (around 200–300 °C) is attributed to the oxidation of the metal components in the system. Oxidation of carbon in all samples occurs in the temperature range characteristic of SWNT. The sample synthesized on the Co–MCM-41 catalysts has two distinct oxidation peaks in the interval 300–700 °C. This shape has been noted before in TGA measurements of SWNT synthesized on Co–MCM-41 and was seen to come mostly from the different displacement of SWNT bundles in the framework (inside or outside the silica pores) [42]. Our multiple TEM observations did not identify any multiwalled carbon nanotubes in the sample. The TGA was also repeated after treatment with sodium hydroxide solution to remove the silica template and hydrochloric acid to remove some of the metal particles not coated with carbon. Consistent with our hypothesis, the double peak shape converted to one single peak (Figs. S7–S9 of Supporting information). This showed that different tube bundles placement in the template and proximity to metal particles is most likely responsible for the double peak shape of the Co–MCM-41 in DTG.

The maximum rate of oxidation occurs at different temperatures for SWNT synthesized on the different catalysts. This can be seen as an effect of a number of factors. The presence of metal components in the system can induce pre-combustion effects in SWNT [48]. The total metal loading in the bimetallic catalysts is twice that of the monometallic catalysts; therefore, the pre-combustion effects are expected to be more important, i.e. a lower maximum oxidation rate temperature is expected. Another factor is the size of the carbon nanotubes. Since the size of the nucleating particles is smaller in the bimetallic catalysts, it is expected that

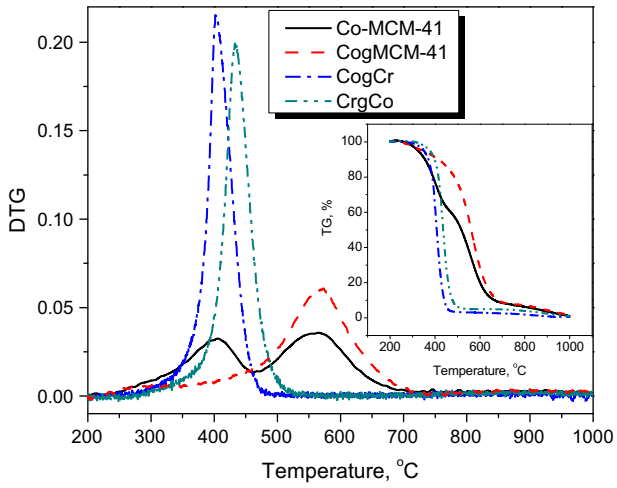


**Fig. 10.** Inverted derivative of the weight variation with temperature during SWNT oxidation normalized per mg carbon. Inset of the thermogravimetric weight loss during temperature ramp.

the average diameter of the synthesized SWNT is smaller. Smaller tubes are expected to oxidize at lower temperatures [48]. Bundling effects of SWNT are also of importance since larger bundles will be more resistant to oxidation.

The total carbon yield has been determined from the weight variation of the sample assuming that only carbon oxidized since the other two constituents of the system (silica and metals) are stable over this temperature interval and is expressed as the mass of total deposited carbon per mass of catalyst in Table 6. The selectivity for each carbonaceous species was determined based on the weight variation in its assigned oxidation interval and represents an approximate value.

A significant increase in the carbon yield is noted with the addition of Cr. The yield for both bimetallic catalysts is around the same value 31–33%. When compared to the monometallic catalysts, an increase by a factor of 2 from the Co–MCM-41 and a factor of almost 3 from the CogMCM-41 is noted. Selectivity toward carbon nanotubes is also increased in the bimetallic catalysts. The high yield is a consequence of the presence of Cr in the catalysts. As noted before, the anchoring effect prevents sintering of Co particles. A larger fraction of the Co is therefore stabilized in the range favorable for SWNT nucleation.

Stability of the template also plays an important role in the yield increase. A CoCr–MCM-41 bimetallic catalyst synthesized by co-incorporation of the same amount of metal as in the CogCr and CrgCo catalysts showed a very poor structure due to the collapse of the MCM-41. The carbon yield on this catalyst was under 10% (Table S2 of Supporting information).

A note should be made that in our previous investigations of CoCr–MCM-41 catalysts synthesized by isomorphous substitution of both metals in the framework within a 3% total metal load limit, the highest carbon yield obtained was 9.5% [14].

**Table 6**
Thermal Gravimetric Analysis results for the as-reacted Co–MCM-41, CogMCM-41, CogCr and CrgCo catalysts.

| Catalyst | Carbon yield (%) | Selectivity (%) | | |
|---|---|---|---|---|
| | | Amorphous carbon | SWNT | Graphite |
| Co–MCM-41 | 14.8 | 2.8 | 91.5 | 5.7 |
| CogMCM-41 | 11.3 | 5.3 | 85.8 | 8.9 |
| CogCr | 33.3 | 3.0 | 95.8 | 1.2 |
| CrgCo | 30.8 | 1.1 | 96.3 | 1.6 |

Raman Spectroscopy represents a good probe into the structure of the quasi one-dimensional SWNT [52]. Fig. 11 shows the Raman spectra collected at 785-nm laser wavelength for the as-reacted catalysts. The spectra collected at 532-nm laser wavelength are shown in Fig. S10 of Supporting information. The low frequency Radial Breathing Mode (RBM) under 450 $cm^{-1}$, the defect-induced D-band around 1300 $cm^{-1}$, and the 1D to 2D graphene sheet folding–induced G-band around 1600 $cm^{-1}$ provide information on the diameter and electronic properties of these materials [53,54]. The RBM region is particularly of interest since it has a strong dependence of the tube diameter.

The electronic density of states of SWNT displays van Hove singularities in the valence and conduction bands [55]. The Raman signal of nanotubes is resonantly enhanced if the excitation energy matches the separations between the pairs of Van Hove singularities in the one-dimensional electronic density of states of the SWNT. A Raman spectrum will therefore only show a subset of all the SWNT identities present in a given sample. As observed by Pimenta et al. [56], a red shift in energy from the isolated nanotubes that is dependent on the tube diameter can occur for bundled SWNT when compared to isolated ones due to laser heating. The same authors recommend the formula RBM ($cm^{-1}$) = 219/($d_t$ + 15) for determining the diameter of SWNT from the position of the RBM peaks where $d_t$ is the tube diameter in nm.

At this excitation wavelength, two RBM signals are dominant in the monometallic samples corresponding to diameters of 0.75–0.9 nm. In the bimetallic samples, these two signals become suppressed, and a dominant peak appears at higher RBM corresponding to a diameter of around 0.57 nm. In accordance with the determined average particle size, the SWNT distribution in the bimetallic samples shifted to lower values.

The Intermediate Frequency Modes between 600 and 1200 $cm^{-1}$ are also of interest. In the monometallic samples, a few weak peaks appear in the interval 800–1200. In the bimetallic samples, these peaks are much more intense and new features develop. Although these features are not yet readily understood, it is believed that their intensity will be greater for those nanotubes in which the $E_{11}$ and $E_{22}$ transition energies are close in value such as near-zigzag tubes. The intensity of the IFM's was also seen to increase with decreasing tube diameter [57].

The G-band mode has a distinct shape for the bimetallic catalysts. It splits with two distinct lower intensity peaks at 1500 and 1540 $cm^{-1}$. As noted by Jorio et al. [58], this is an effect of

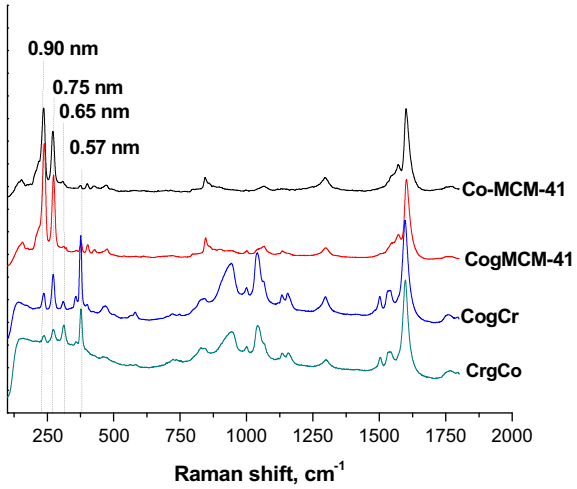


**Fig. 11.** Resonant Raman Spectroscopy of SWNT synthesized on the monometallic and bimetallic catalysts. Position of the most intense RBM features is marked by dotted lines, and the corresponding SWNT diameter is shown.

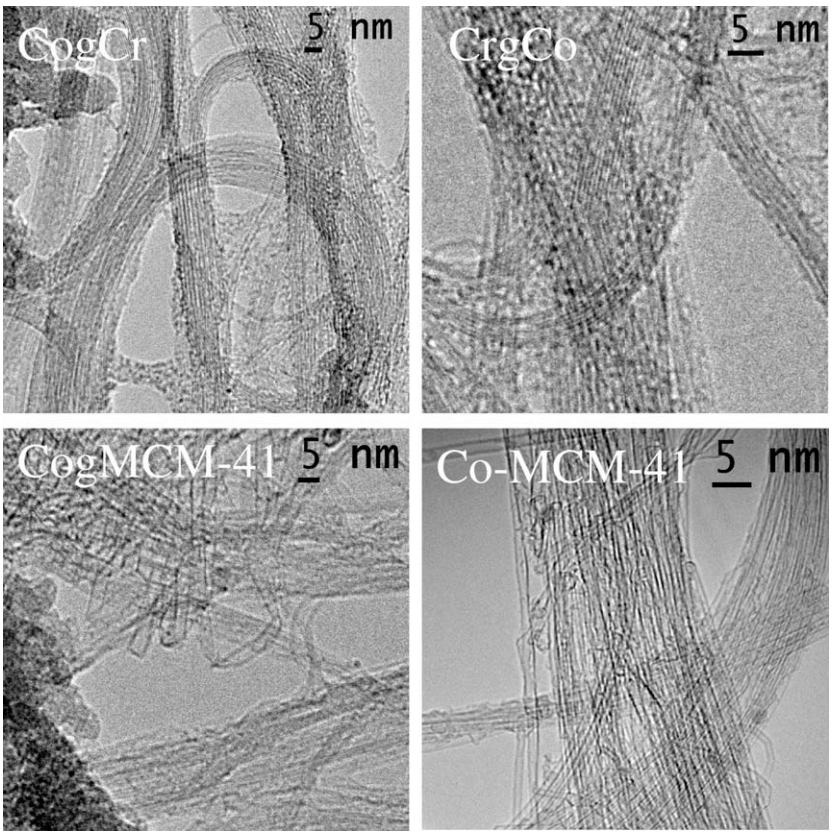


**Fig. 12.** TEM images collected for the as-reacted catalysts without any further purification treatments. Some of the silica template is also visible in the images.

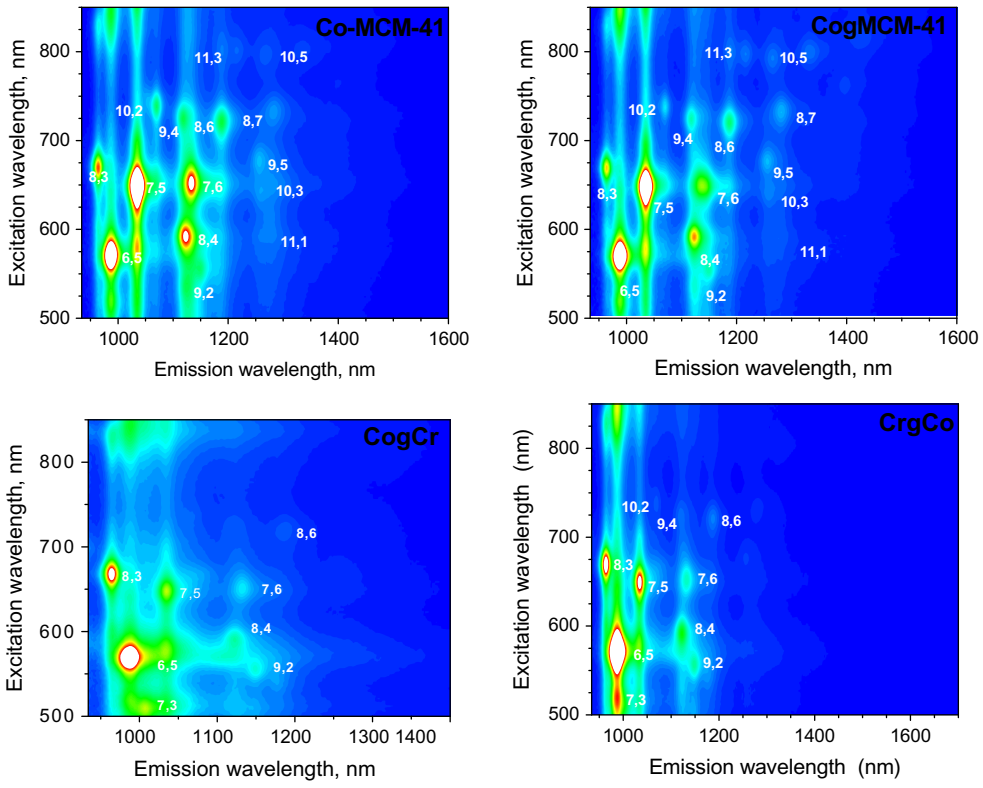


**Fig. 13.** Normalized PLE maps collected for SWNT synthesized on the Co–MCM-41, CogMCM-41, CogCr and CrgCo catalysts.

the decrease in tube diameter. The high curvature of SWNT leads to different force constants for G-band modes with atomic vibrations along the tube axis when compared to modes with vibration in the circumferential direction, which induces splitting of the G-band.

The ratio between the intensity of the G- and D-bands is high in all samples, denoting a low density of defects in the SWNT synthesized on all catalysts, in good agreement with the TGA investigation.

TEM observations of the as-reacted catalysts support the Raman results. SWNT imaged in the bimetallic catalysts had very small diameter mostly between 0.55 and 0.70 nm as seen in Fig. 12. A high abundance of SWNT in the sample was also noted in good agreement with the high yield from the TGA results. Multiple TEM observations did not show any tubes with diameter over 1 nm. The largest tube size distribution was observed for the CogMCM-41 catalyst with tube diameters up to 2.5 nm.

To further investigate the shift in diameter distribution, we have collected photoluminescence data for purified SWNT samples synthesized on the Co–MCM-41, CogMCM-41, CogCr and CrgCo catalysts. The PLE maps are shown in Fig. 13.

Fluorescence spectroscopy represents a good method for identifying most $(n, m)$ semiconducting SWNT and their relative abundance [59,60]. Precise composition analysis is difficult at this time due to the differences in models for the contribution of excitonic processes to the electronic transitions but estimates are possible [59]. Table 7 shows the relative abundance determined from the PLE data for the main $(n, m)$ semiconducting SWNT.

From the analysis of the abundance data in Table 7, it is clear that tubes of smaller diameter are predominant in the bimetallic catalysts as was indicated by the Raman and TEM analysis. For example, the (6, 5) and (8, 3) nanotubes both with diameter under 0.8 nm are more than twice more abundant in the bimetallic samples than in the monometallic ones. Also of interest is the appearance of the (7, 3) nanotube in both bimetallic samples. This tube has the smallest diameter that can be identified with our current fluorescence setup.

Notably, the abundance of semiconducting SWNT with diameter of under 0.8 nm represents 25% of the Co–MCM-41 sample, 30% of the CogMCM-41, 70% of CogCr and 66% of CrgCo. This is in good agreement with the Raman and TEM data identifying a shift in diameter distribution to smaller tubes in the bimetallic catalysts.

A note should be made on the very small tubes identified by Raman and TEM analysis. For example, the most intense RBM peak that appears in the Raman spectra of bimetallic catalysts collected at 785-nm excitation is at 380 $cm^{-1}$ corresponding to the (5, 4) nanotube with a diameter of 0.556 nm [57]. As discussed, the smallest tube we can identify in fluorescence is (7, 3). It is possible that even smaller-diameter SWNT are present in the bimetallic samples.

Small-diameter nanotubes are interesting because their high radius of curvature confers them unusual electronic properties such as superconductivity at higher temperature than larger tubes. High curvature is also associated with properties that vary dramatically with applied force, enabling switches and non-volatile memories [61,62].

**Table 7**
Relative abundance of main semiconducting tubes identified by fluorescence spectroscopy.

| Tube $(n, m)$ | Diameter (nm) | Relative abundance (%) | | | |
|---|---|---|---|---|---|
| | | Co–MCM-41 | CogMCM-41 | CogCr | CrgCo |
| 6, 5 | 0.757 | 15.8 | 21.0 | 32.0 | 36.5 |
| 9, 2 | 0.806 | 4.1 | 3.6 | 5.4 | 4.6 |
| 8, 4 | 0.840 | 11.0 | 9.6 | 6.5 | 6.6 |
| 11, 1 | 0.916 | 1.2 | 1.0 | 0.0 | 0.0 |
| 8, 3 | 0.782 | 9.2 | 8.9 | 23.3 | 16.9 |
| 7, 5 | 0.898 | 24.7 | 29.9 | 13.2 | 14.8 |
| 7, 6 | 0.895 | 11.2 | 7.2 | 4.5 | 4.1 |
| 10, 3 | 0.936 | 1.6 | 1.5 | 0.0 | 0.0 |
| 10, 2 | 0.884 | 4.0 | 2.5 | 0.0 | 1.1 |
| 9, 4 | 0.916 | 4.3 | 3.6 | 0.0 | 1.4 |
| 8, 6 | 0.966 | 4.4 | 4.4 | 1.8 | 1.6 |
| 8, 7 | 1.032 | 1.5 | 2.0 | 0.0 | 0.0 |
| 9, 5 | 0.976 | 1.8 | 2.0 | 0.0 | 0.0 |
| 11, 3 | 1.014 | 1.2 | 2.3 | 0.0 | 0.0 |
| 10, 5 | 1.050 | 0.9 | 1.3 | 0.0 | 0.0 |
| 7, 3 | 0.706 | 0.0 | 0 | 13.0 | 12.3 |

## 4. Conclusion

In conclusion, we have demonstrated a novel synthesis route for bimetallic CoCr–MCM-41 catalysts by combined incorporation and grafting of two metals in the MCM-41 framework. We have substantially increased the maximum allowed metal loading in the MCM-41 catalytic system while maintaining the structural properties of the MCM-41 framework. The order or method in which the two metals are added to the MCM-41 structure did not appear to make any difference in their catalytic properties.

High dispersion of Co nanoparticles was formed and found to be stable in high-temperature reactive environments. These catalysts were shown to both increase SWNT yield and allow synthesis of narrow diameter distributions of small SWNT.

## Acknowledgments

We gratefully acknowledge financial support form NSF D01521 and MURI L00096.

We thank the NSLS beamlines X18B and X23A2 – Brookhaven Laboratory for use of their facilities and acknowledge Prof. Nebojsa Marinkovic and Prof. Bruce Ravel for their support in collecting the EXAFS data.

## Appendix A. Supplementary material

Supplementary data associated with this article can be found, in the online version, at doi:10.1016/j.jcat.2010.02.021.

## References

[1] S.J. Tans, A.R. Verschueren, C. Dekker, Nature 393 (1998) 49–52.
[2] J. Nie, W. Quian, Q. Zhang, Q. Wen, F. Wei, J. Phys. Chem. C 113 (2009) 20178.
[3] R.H. Baughman, A.A. Zakhidov, W.A. Heer, Science 297 (2002) 787–792.
[4] J. Gonzalez, Phys. Rev. B 67 (2003) 014528-1–014528-12.
[5] K.P. Bohnen, R. Heid, C.T. Chan, J. Phys.: Condens. Matter 21 (2009) 084206–084213.
[6] R. Saito, G. Dresselhaus, M.S. Dresselhaus, Phys. Rev. B 61 (2000) 2981–2990.
[7] S.J. Kang, C. Kocabas, T. Ozel, M. Shim, N. Pimparkar, M.A. Alam, S.V. Rotkin, J.A. Rogers, Nat. Nanotechnol. 2 (2007) 230–236.
[8] J.E. Herrera, L. Balzano, B. Armando, W.E. Alvarez, D.E. Resasco, J. Catal. 204 (2001) 129–145.
[9] J.E. Herrera, D.E. Resasco, J. Phys. Chem. B 107 (2003) 3738–3746.
[10] X. Li, X. Tu, S. Zaric, K. Welsher, W. Seo, W. Zhao, H. Dai, J. Am. Chem. Soc. 129 (2007) 15770–15771.
[11] A.M. Cassel, J.A. Raymakers, J. Kong, H.J. Dai, J. Phys. Chem. B 103 (1999) 6484–6492.
[12] M. Takizawa, S. Bandow, M. Yudasaka, Y. Ando, H. Shimoyama, S. Iijima, Chem. Phys. Lett. 326 (2000) 351–357.
[13] A.M. Cassell, J.A. Raymakers, J. Kong, H. Dai, J. Phys. Chem. B 103 (1999) 6484–6492.
[14] C. Zoican Loebick, S. Derrouiche, F. Fang, N. Li, G. Haller, L. Pfefferle, Appl. Catal. A 368 (2009) 40–49.
[15] C. Zoican Loebick, D. Abanulo, M. Majewska, G. Haller, L. Pfefferle, Appl. Catal. A, in press, doi: 10.1016/j.apcata.2009.12.010.
[16] S. Lim, D. Ciuparu, C. Pak, F. Dobek, Y. Chen, D. Harding, L. Pfefferle, G. Haller, J. Phys. Chem. B 107 (2003) 11048–11056.
[17] S. Lim, D. Ciuparu, Y. Yang, G. Du, L. Pfefferle, G. Haller, Microporous Mesoporous Mater. 101 (2007) 200–206.
[18] Y. Chen, D. Ciuparu, S. Lim, G. Haller, L. Pfefferle, Carbon 44 (2006) 67–78.

[19] C. Wang, S. Lim, G. Du, C. Zoican Loebick, N. Li, S. Derrouiche, G. Haller, J. Phys. Chem. C 113 (2009) 14863–14871.
[20] S.L. Soled, E. Iglesia, R.A. Fiato, J.E. Baumgartner, H. Vroman, S. Misto, Top. Catal. 26 (2003) 101.
[21] D.J. Duvenhage, N.J. Coville, Catal. Lett. 104 (2005) 129.
[22] S.Y. Lin, D.H. Kim, S.Y. Ha, Catal. Lett. 122 (2008) 295.
[23] X. Guo, Y. Li, R. Shi, Q. Liu, E. Zhan, W. Shen, Appl. Catal. A 371 (2009) 108.
[24] S. Lim, Y. Yang, D. Ciuparu, C. Wang, Y. Chen, L. Pfefferle, G.L. Haller, Top. Catal. 34 (2005) 31–40.
[25] Y. Chen, D. Ciuparu, S. Lim, G. Haller, L. Pfefferle, J. Catal. 225 (2004) 453–459.
[26] P.J. Branton, P.G. Hall, K.S. King, H. Reichert, F. Schuth, K.K. Unger, J. Chem. Soc., Faraday Trans. 90 (1994) 2965–2967.
[27] P.B. Amama, S. Lim, D. Ciuparu, L. Pfefferle, G.L. Haller, Microporous Mesoporous Mater. 81 (2005) 191–200.
[28] C.T. Kresge, M.E. Loonowicz, W.J. Roth, J.C. Vartuli, J.S. Beck, Nature 359 (1992) 710–714.
[29] F. Beland, A. Baidei, M. Ronning, D. Nicholson, L. Bonneviot, Phys. Chem. Chem. Phys. 1 (1999) 605–613.
[30] G. Jacobs, Y. Ji, B.H. Davis, D. Cronauer, A.J. Kropf, C.L. Marshal, Appl. Catal. A 333 (2007) 177–191.
[31] D. Ciuparu, P. Haider, M. Fernandez-Garcia, Y. Chen, S. Lim, G.L. Haller, L. Pfefferle, J. Phys. Chem. B 109 (2005) 16332–16339.
[32] C. Pak, G.L. Haller, Microporus Mesoporous Mater. 48 (2001) 165–170.
[33] B. Weckhuysen, R. Schoonheydt, J. Jehng, I. Wachs, S. Cho, R. Ryoo, S. Kijlstra, E. Poels, J. Chem. Soc., Faraday Trans. 18 (1991) 3245.
[34] J. Pamparnot, S. Kaewkun, P. Praserthdam Jr., J. Goodwin Jr., Catal. Lett. 91 (2003) 95–102.
[35] J. Slockzynski, J. Janas, T. Machej, J. Rynkowski, J. Stoch, Appl. Catal. B: Environ. 24 (2000) 45–60.
[36] S. Lim, D. Ciuparu, C. Pak, F. Dobek, Y. Chen, D. Harding, L. Pfefferle, G. Haller, J. Phys. Chem. B 107 (2003) 11048–11056.
[37] J.A. Rodriguez, J.C. Hanson, S. Cahturvedi, J. Chem. Phys. 112 (2000) 935–944.
[38] J.A. Rodriguez, J.C. Hanson, S. Chaturvedi, J. Phys. Chem. B 104 (2000) 8145–8152.
[39] K. Eda, Y. Uno, N. Nagai, N. Sotani, M. Stanley Whittingham, J. Solid State Chem. 178 (2005) 2791–2797.
[40] K. Takehira, Y. Ohishi, T. Shisido, T. Kawabata, K. Takaki, Q. Zhang, Y. Wang, J. Catal. 224 (2004) 404–416.
[41] Y. Wang, Y. Ohishi, T. Shishido, Q. Zhang, W. Yang, Q. Guo, H. Wan, K. Takehira, J. Catal. 220 (2003) 347–357.
[42] S. Lim, N. Li, F. Fang, M. Pinault, C. Zoican, C. Wang, T. Fadel, L. Pfefferle, G. Haller, J. Phys. Chem. C 112 (2008) 12442–12449.
[43] G. Agostini, E. Groppo, S. Bordiga, A. Zecchina, C. Prestipino, F. D'Acapito, E. Van Kimmenade, P. Thuene, J. Niemantsverdriet, C. Lamberti, J. Phys. Chem. C 111 (2007) 16437–16442.
[44] F. Dign, A. Rosen, K. Bolton, J. Chem. Phys. 121 (2004) 2775–2778.
[45] F. Dign, A. Rosen, K. Bolton, Chem. Phys. Lett. 393 (2004) 309–313.
[46] G. Lolli, L. Zhang, L. Balzano, N. Sakulchaicharoen, Y. Tan, D.E. Resasco, J. Phys. Chem. C 110 (2006) 2108.
[47] Y. Miyauchi, S. Chiashi, Y. Marukami, S. Maruyama, Chem. Phys. Lett. 387 (2004) 198.
[48] B. Kitiyanan, W.E. Alvarez, J.H. Harwell, D.E. Resasco, Chem. Phys. Lett. 317 (2000) 497.
[49] C. Lee, J. Park, Y. Huh, L.Y. Lee, Chem. Phys. Lett. 343 (2001) 33–37.
[50] M. Zhang, M. Yudasaka, A. Koshio, S. Iijima, Chem. Phys. Lett. 364 (2002) 420–426.
[51] B.J. Landi, S.D. Cress, C.M. Evans, R.P. Rafaelle, Chem. Mater. 17 (2005) 6819–6824.
[52] M. Dresselhaus, G. Dresselhaus, A. Jorio, A. Souza Filho, R. Saito, Carbon 40 (2002) 2043–2049.
[53] M. Dresselhaus, G. Dresselhaus, M. Hofman, Vib. Spectrosc. 45 (2007) 71–78.
[54] M.S. Dresselahus, G. Dresselhaus, A. Jorio, J. Phys. Chem. C 111 (2007) 17887–17892.
[55] R. Saito, G. Dresselhaus, M.S. Dresselhaus, Physical Properties of Carbon Nanotubes, Imperial College Press, London, 1998.
[56] M.A. Pimenta, A. Gomes, C. Fantini, L.G. Cancado, P.T. Araujo, I.O. Maciel, A.P. Santos, C.A. Furtado, V.S. Peressinotto, F. Plentz, A. Jorio, Physica E 37 (2007) 88–94.
[57] N. Li, X. Wang, F. Ren, G. Haller, L. Pfefferle, J. Phys. Chem. C 113 (2009) 10070–10078.
[58] A. Jorio, A.G. Souza Filho, G. Dresselhaus, M.S. Dresselhaus, A.K. Swan, M.S. Unlu, B.B. Goldberg, M.A. Pimenta, J.H. Hafner, C.M. Lieber, R. Saito, Phys. Rev. B 65 (2002) 155412-1–155412-9.
[59] S.M. Bachilo, L. Balzano, J.E. Herrera, F. Pompeo, D.E. Resasco, R.B. Weisman, J. Am. Chem. Soc. 125 (2003) 11186–11187.
[60] Y. Oyama, R. Saito, K. Sato, J. Jiang, Ge. Samsonitze, A. Gruneis, Y. Miyauchi, S. Maruyama, A. Jorio, G. Dresselhaus, M. Dresselhaus, Carbon 44 (2006) 873–879.
[61] Z.K. Tang, L. Zhang, N. Wang, X.X. Zhang, G.H. Wen, G.D. Li, J.N. Wang, C.T. Chan, P. Sheng, Science 292 (2001) 2462.
[62] E. Perfetto, J. Gonzalez, J. Phys.: Condens. Matter 18 (2006) S2105.